Research Article
Journal of Geophysical Research: Oceans
DOI 10.1002/2015JC011597

Forcing of the Overturning Circulation across a Circumpolar Channel by Internal Wave Breaking

Maria B. Broadbridge,[1] **Alberto C. Naveira Garabato,**[2] **A. J. George Nurser** [3]

[1]Department of Physics, Imperial College, London, UK.

[2]University of Southampton, National Oceanography Centre, Southampton, United Kingdom

[3]National Oceanography Centre, Southampton, United Kingdom

Key Points:

- The breaking of topographially generated internal lee waves enhances diapycnal diffusivity.
- The diapycnal mixing generated by the simulated eddy field regulates the deep overturning.
- Mesoscale eddies displace isopycnals vertically and set the vertical structure of the deep MOC.

Corresponding author: M. B. Broadbridge, m.broadbridge@imperial.ac.uk

Received: Dec 21, 2015; Revised: May 03, 2016; Accepted: Jun 21, 2016

Abstract

The hypothesis that the impingement of mesoscale eddy flows on small-scale topography regulates diapycnal mixing and meridional overturning across the deep Southern Ocean is assessed in an idealised model. The model simulates an eddying circumpolar current coupled to a double-celled meridional overturning with properties broadly resembling those of the Southern Ocean circulation, and represents lee wave-induced diapycnal mixing using an online formulation grounded on wave radiation theory. The diapycnal mixing generated by the simulated eddy field is found to play a major role in sustaining the lower overturning cell in the model, and to underpin a significant sensitivity of this cell to wind forcing. The vertical structure of lower overturning is set by mesoscale eddies, which propagate the effects of near-bottom diapycnal mixing by displacing isopycnals vertically.

1 Introduction

The Southern Ocean plays a pivotal role in the global overturning circulation. The absence of continental barriers in the latitude band of Drake Passage permits the existence of the Antarctic Circumpolar Current (ACC), which is supported geostrophically by sloping isopycnals and serves as the main conduit for oceanic exchanges between the three major ocean basins. Coupled to this eastward flow, a meridional circulation exists in which deep water of predominantly North Atlantic origin together with Indian and Pacific Deep waters upwells along the poleward-shoaling isopycnals of the ACC and is returned equatorward in a double overturning cell [see *Rintoul and Garabato*, 2013; *Talley*, 2013, and references therein]. Our present understanding of the dynamics regulating these zonal and meridional circulations and their coupling owes much to studies of idealised models of (or including) a zonally re-entrant channel, and to residual-mean analyses of realistic models [e.g. *Marshall and Radko*, 2003; *Hallberg and Gnanadesikan*, 2006; *Abernathey et al.*, 2011; *Dufour et al.*, 2012; *Meredith et al.*, 2012; *Marshall and Speer*, 2012; *Morrison and McC. Hogg*, 2013; *Thompson and Naveira Garabato*, 2014]. This literature unanimously emphasises the significance of mesoscale eddies, generated by baroclinic instability of the ACC, in both closing the zonal momentum budget and inducing meridional overturning, particularly at open-channel depths where no time-mean geostrophic flow may exist.

More recently, evidence has emerged suggesting that the Southern Ocean eddy field may impact meridional overturning beyond its widely acknowledged role in effecting adiabatic, along-isopycnal transport. This evidence comes from two distinct lines of work. First, theoretical es-

timates of the rate of generation of internal lee waves by eddy flows impinging on small-horizontal-scale (O(1 – 10 km)) topography indicate that this mechanism may be a significant contributor to the dissipation of the eddy field [*Nikurashin and Ferrari*, 2010a,b; *Scott et al.*, 2011]. Second, fine- and microstructure measurements across Southern Ocean areas of complex topography reveal elevated (typically by at least one order of magnitude relative to oceanic background values) rates of turbulent dissipation and diapycnal mixing in the deepest 1000 - 2000 m of those regions, linked to the eddy-induced generation and breaking of lee waves [*Naveira Garabato et al.*, 2004; *St. Laurent et al.*, 2012; *Brearley et al.*, 2013; *Sheen et al.*, 2013, 2014; *Waterman et al.*, 2013]. As diapycnal mixing has been shown to be a rate-setting process in deep-ocean overturning [e.g. *Ito and Marshall*, 2008; *Nikurashin and Vallis*, 2011], and eddy kinetic energy in the ACC to be highly sensitive to wind perturbations [see *Meredith et al.*, 2012, and references therein], the hypothesis is prompted that the eddy field's impingement on small-scale topography (and, by extension, wind forcing) regulates diapycnal mixing and meridional overturning across the deep Southern Ocean.

In this paper, we assess the validity of this hypothesis in an idealised model of an eddying zonal channel flow coupled to a double-celled meridional overturning with properties broadly resembling those of the Southern Ocean circulation. Lee wave-induced diapycnal mixing is represented in the model using an online formulation grounded on wave radiation theory. We show that the lee wave-induced diapycnal mixing generated by the simulated eddy field is a major factor in sustaining the lower overturning cell in the model, and that it underpins a significant sensitivity of this cell to wind forcing perturbations.

2 Parameterization of lee wave-induced diapycnal mixing

Our parameterization of the spatio-temporally variable diapycnal diffusivity due to lee wave breaking, $\kappa_{\rm iw}$, takes the form

$$\kappa_{\rm iw}(x,y,z,t)N^2(x,y,z,t) = -\mathcal{B}_{\rm iw}(x,y,z,t) = \rho_0^{-1}\Gamma\, G(x,y,t)F(z) \qquad (1)$$

where N is the buoyancy frequency, $\mathcal{B}_{\rm iw}(x,y,z,t)$ is the turbulent buoyancy flux driven by breaking internal waves, ρ_0 is density, $\Gamma = 0.2$ is the mixing efficiency for shear-driven turbulence [*Osborn*, 1980]; G is the rate of energy transfer from mesoscale eddy motions, resolved in the model, to the unresolved lee wave field; and F is a vertical structure function of the rate of IW energy dissipation. G is expressed as a function of near-bottom horizontal velocity and N, and involves a 2-d spectral description of the unresolved small-scale bottom topography

implicated in lee wave generation. Its specification, included below for completeness, follows the wave radiation theory-based formulation of *Scott et al.* [2011].

We have chosen the canonical value for mixing efficiency for our setup as postulated by *Osborn* [1980]. In a recent study, *de Lavergne et al.* [2015] have explored the impact of variable mixing efficiency on the deep overturning circulation and found that a mixing efficiency corresponding to $\Gamma = 0.2$ is a reasonable assumption, although it may overestimate the near-bottom eddy diffusivities due to the weak stratification near the bottom boundary.

In this work, we will assume that the lee waves generated by geostrophic flow over topography do not experience significant horizontal propagation (relative to the model grid spacing) and that they break at some level within the water column, such that the depth-integrated turbulent kinetic energy dissipation (ϵ) matches the vertical flux of energy associated with the waves at generation (G), i.e.

$$\int_{-H}^{0} \epsilon(x, y, z, t)\ dz = G(x, y, t). \tag{2}$$

The first assumption follows from the intrinsic role that the geostrophic flow plays in the generation and persistence of the lee waves, which locks them to the horizontal proximity of their generation site [e.g. *Ferrari and Nikurashin*, 2010]. The second reflects our present lack of knowledge on the characteristic evolution of lee waves as they propagate vertically, and the high likelihood of eventual breaking, particularly in the presence of nonlinearity in the internal wave field and buoyancy scaling effects (see *Naveira Garabato et al.* [2004] and *Nikurashin and Ferrari* [2010a] for a discussion). Note, though, that if the dissipation of the lee waves within the bottom part of the water column is not complete, the depth integral of ϵ will be reduced proportionally.

The transfer of energy into the internal lee waves, G, is of course associated [cf. *Naveira Garabato et al.*, 2013] with a loss of energy from the resolved flow via a wave drag $-\boldsymbol{\tau}_{\mathrm{iw}}$, consistent with $-\mathbf{u} \cdot \boldsymbol{\tau}_{\mathrm{iw}} = G$. We did not choose to include this in the following numerical simulations since we wished to consider the dynamic effect of the IW mixing in isolation.

2.1 Parameterization of lee wave power

The generation of internal lee waves by geostrophic flow over topography has been studied from a theoretical perspective by *Bell* [1975], *Gill* [1982] and *Nikurashin and Ferrari* [2010a], amongst others. Adopting the traditional approximation of ignoring the horizontal components

of the Coriolis force, the linearized density equation and non-hydrostatic, vertical momentum equation provide a relation between pressure and vertical velocity. For small-amplitude sinusoidal topography, the vertical velocity is imposed by the kinematic boundary condition, and one can solve for the vertical flux of energy resulting from the pressure–topographic slope correlation. The energy flux is non-zero if the oscillations generated by flow over topography can propagate as waves, i.e. if their intrinsic frequency $\sigma = \mathbf{k} \cdot \mathbf{u}$ (where $\mathbf{k} = (k, l)$ is the horizontal wavenumber of the topography and $\mathbf{u} = (u, v)$ is the near-bottom horizontal velocity) lies between the inertial (f) and buoyancy (N) frequencies, $|f| < |\sigma| < N$. The energy extracted from the background flow is carried upward by the waves as they radiate away from the boundary, and dissipated when the waves break. Representing the topography by a two-dimensional power spectrum $P(k, l)$ that varies slowly on spatial scales much larger than the wavelengths of lee waves, it may be shown that the net vertical flux of energy resulting from the sum of all contributions within the internal wave band is given by

$$G_{\mathrm{lin}}(x, y, t) = \frac{\rho_0}{4\pi^2} \int_{-\infty}^{\infty} \int_{-\infty}^{\infty} S(\sigma) \frac{\sigma}{\sqrt{k^2 + l^2}} P(k, l) \sqrt{N^2 - \sigma^2} \sqrt{\sigma^2 - f^2} \, dk \, dl, \tag{3}$$

where ρ_0 is the fluid density and

$$S(\sigma) = \begin{cases} 1 & \text{if} \quad |f| < |\sigma| < N; \ \sigma > 0, \\ -1 & \text{if} \quad |f| < |\sigma| < N; \ \sigma < 0, \\ 0 & \text{otherwise} \end{cases}$$

The linear theory above describes well the generation of lee waves when the topography has small amplitude in the sense of

$$\frac{1}{\mathrm{Fr}} \equiv \frac{\mathcal{H} N}{\mathcal{U}} \leq \frac{1}{\mathrm{Fr}_c}, \tag{4}$$

where Fr is the Froude number of the flow, $\mathcal{U}$ is a background velocity scale, $\mathcal{H}$ is the amplitude of the topographic variations, and Fr_c is a critical Froude number. As topographic amplitude and buoyancy frequency increase or as background velocity decreases, the flow becomes increasingly blocked by the topography, leading to substantially less lee wave radiation than indicated by (3). Empirical corrections for this phenomenon have been put forward and tested with laboratory experiments and numerical simulations. These are reviewed by *Scott et al.* [2011] and will not be discussed here. We follow *Scott et al.* [2011] in adopting a correction for topographic blocking of the form

$$G(x, y, t) = G_{\mathrm{lin}}(x, y, t) \frac{\mathcal{L}}{\pi} \left(\arccos(1 - 2\mathcal{L}) - 2(1 - 2\mathcal{L}) \sqrt{\mathcal{L}(1 - \mathcal{L})} \right), \tag{5}$$

where

$$\mathcal{L} = 1, \quad \mathrm{Fr}^{-1} \leq \mathrm{Fr}_c^{-1};$$
$$\mathcal{L} = \tfrac{\mathrm{Fr}}{\mathrm{Fr}_c}, \quad \mathrm{Fr}^{-1} > \mathrm{Fr}_c^{-1}.$$

As in *Scott et al.* [2011], Fr_c^{-1} is taken as 0.7, and the amplitude of the topography in (5) is defined as

$$\mathcal{H}^2 = \frac{1}{4\pi^2} \int_{-\infty}^{\infty} \int_{-\infty}^{\infty} |S(\sigma)| P(k,l)\, dk\, dl. \tag{6}$$

This is a metric of the amplitude of the topographic variations contributing to lee wave generation, and is therefore time-dependent (through σ). Our results are insensitive (to better than 1%) to the choice of other possible corrections in the literature. See *Naveira Garabato et al.* [2013] for a discussion of the uncertainties surrounding these corrections.

Following *Goff and Jordan* [1988, 1989], we adopt a representation of the topographic power spectrum of the form

$$P(k,l) = 4\pi\nu \frac{h_{rms}^2}{k_n k_s} \left(\frac{K^2}{k_s^2} \cos^2(\theta - \theta_s) + \frac{K^2}{k_n^2} \sin^2(\theta - \theta_s) + 1 \right)^{-(\nu+1)}, \tag{7}$$

where k_s and k_n are the wavenumbers in the strike and normal directions, respectively, with $k_n \geq k_s$; θ_s measures the angle clockwise from true north to the strike direction; $\theta = \arctan(k/l)$ is the angle clockwise from true north of the wavenumber vector; the Hurst number ν indicates the steepness of the spectrum at high wavenumbers; and h_{rms} is the root-mean-square topographic height variability, defined such that

$$\int_{-\infty}^{\infty} \int_{-\infty}^{\infty} P(k,l)\, dk\, dl = h_{\mathrm{rms}}^2.$$

In our model experiments, the parameters (k_s, k_n, ν, θ_s) are set to the constant values (8×10^{-4} rad m^{-1}, 3×10^{-5} rad m^{-1}, 0.95, 20°) characteristic of abyssal hills [*Goff and Arbic*, 2010]. However, the sensitivity of the modelled circulation to changes in h_{rms} is investigated, as this is the most significant topographic parameter in determining G in the ocean [*Scott et al.*, 2011].

2.2 Depth profile of lee-wave induced mixing

A profile of the rate of turbulent kinetic energy dissipation is defined at each horizontal model grid point as

$$\epsilon(x,y,z,t) = G(x,y,t)F(z), \tag{8}$$

where F is a vertical structure function characterising the rate of breaking of the lee waves propagating upward from the bottom. A physical model for F for lee waves, analogous to that developed for internal tides [*Polzin*, 2009], is not yet available, so we follow the *ad hoc* approach of *St. Laurent et al.* [2002] and prescribe F as a simple analytical function. We choose a linear vertical structure of the form

$$F(z) = \frac{2(h^* - H - z)}{h^{*2}}, \tag{9}$$

where h^* is set to 1000 m on the basis of fine- and microstructure estimates of lee wave-induced ϵ in the ACC, which suggest that the dissipation is focussed within 1000 - 2000 m of the seafloor[*St. Laurent et al.*, 2012; *Waterman et al.*, 2013; *Sheen et al.*, 2013]. The vertical integral of F is 1, consistent with the complete local dissipation of lee-waves (2) within a height h^* off the bottom in the same grid point, i.e. lee wave radiation and breaking are assumed to be local in the horizontal [*Nikurashin and Ferrari*, 2010a]. Note that this linear turbulent buoyancy flux profile implies strong near-bottom buoyancy gain, and uniform weaker compensating buoyancy loss throughout the depth-range between the bottom $z = -H$ and the depth $z = -H+h^*$ where the buoyancy flux associated with the breaking internal waves is assumed to disappear (in our case the bottom 1000 m); thus the buoyancy gain from the internal wave forcing is

$$B_{\rm iw} = -\frac{\partial \mathcal{B}_{\rm iw}}{\partial z} \quad = \begin{cases} h^* B_{\rm iw0} \delta(z+H) & \text{at the bottom,} \\ B_{\rm iw0} & -H < z < -H + h^*, \\ 0 & z > -H + h^* \end{cases} \tag{10}$$

where

$$B_{\rm iw0} = -\left.\mathcal{B}_{\rm iw}\right|_{z=-H} h^{*-1} = 2G\Gamma\rho_0^{-1} h^{*-2} \tag{11}$$

is the interior diapycnal buoyancy flux convergence.

Finally, we invoke the Osborn – Cox relation [*Osborn and Cox*, 1972] to define a diapycnal diffusivity, κ, as

$$\kappa = \frac{\Gamma}{\rho_0}\frac{\epsilon(x,y,z,t)}{N^2(x,y,z,t)} = \frac{\Gamma}{\rho_0}\frac{G(x,y,t)F(z)}{N^2(x,y,z,t)}, \tag{12}$$

where $\Gamma = 0.2$ is a mixing efficiency for shear-driven turbulence.

3 Model configuration and experiments

The MITgcm [*Marshall et al.*, 1997a,b] is configured to simulate a hydrostatic flow in a three-dimensional, flat-bottom, zonally re-entrant channel on a β plane, intended as an idealised representation of an ACC-like circumpolar current [similar to e.g. *Abernathey et al.*, 2011].

The model configuration is summarised by Figure 1. The channel has a zonal extent of 1000 km, a meridional extent (L_y) of 1600 km, and a depth (H) of 3000 m. A horizontal resolution of 5 km is adopted to resolve the first baroclinic deformation radius, which is approximately 10 km in the model domain. The model has 40 vertical levels spaced at intervals ranging from 10 m near the surface to 101.5 m near the bottom. The channel is bounded by a solid wall to the south and by an open boundary to the north, where weak relaxation to an exponential temperature profile, decaying from 6°C at the surface to 0.2°C at the bottom, is applied over a 25-km-wide sponge layer with a tapered (northward- and downward- decreasing) time scale of 30 days at the boundary and about 960 days at the weakest point in the deep interior. This relaxation crudely represents water mass transformations north of the channel, analogous to those in the basins north of the Southern Ocean in the real world, in a much less computationally expensive manner than explicit simulation of a northern basin and the tapering timescales facilitate a smooth forcing towards the channel interior. The model has a linear equation of state and a constant salinity of 34.5.

The model is initialised from a state of rest and a uniform temperature of 2°C, and forced with an eastward wind stress $\tau(y) = \tau_0 \sin(\pi y/L_y)$, where y is meridional distance and τ_0 is the maximum eastward wind stress. This is an idealised representation of the Southern Hemisphere westerlies. The momentum input by the wind is balanced by quadratic bottom drag with a constant coefficient of 0.01. This value, which is roughly five times larger than a realistic coefficient [e.g. *Naveira Garabato et al.*, 2013], prevents the development of an overly barotropic zonal flow that occurs in the absence of topographically blocked geostrophic contours [*Olbers et al.*, 2004]. Diffusion of momentum is effected via horizontal Laplacian and biharmonic viscosity coefficients of 12 $m^2\ s^{-1}$ and 9×10^8 $m^4\ s^{-1}$, respectively, and via a vertical viscosity coefficient of 3×10^{-4} $m^2\ s^{-1}$. The model is also forced by a meridionally variable heat flux $Q(y) = Q_0 \cos(1.5\pi y/L_y) - \langle Q_0 \cos(1.5\pi y/L_y)\rangle$, where $Q_0 = 10$ W m^{-2} and angled brackets indicate a meridional average. As well as ensuring that no net buoyancy is added to the domain, this yields buoyancy loss near the channel's northern and southern edges and buoyancy gain over the centre, in line with the pattern of zonal-mean buoyancy forcing of the Southern Ocean [*Speer et al.*, 2000]. Lateral diffusion of temperature is effected by a weak skew-diffusive Gent-McWilliams [*Gent and McWilliams*, 1990; *Griffies*, 1998] flux with a diffusivity of 10 $m^2\ s^{-1}$, representing sub-grid-scale eddies.

The explicit vertical diffusion is

$$D_v = \frac{\partial}{\partial z}\left(\kappa_0 \frac{\partial T}{\partial z}\right) + \frac{\partial}{\partial z}\left(\kappa_{\mathrm{KPP}} \frac{\partial T}{\partial z}\right) + D_{\mathrm{KPP-nonlocal}} + \frac{\partial}{\partial z}\left(\kappa_{\mathrm{iw}} \frac{\partial T}{\partial z}\right), \qquad (13)$$

where κ_0 is a constant background diapycnal diffusivity set to 10^{-5} m^2 s^{-1}s; D_{KPP} is the diffusivity associated with the K-Profile parameterisation of mixing in the surface mixed layer and a Richardson number-dependent mixing in the interior [*Large et al.*, 1994]; $D_{\mathrm{KPP-nonlocal}}$ represents nonlocal KPP fluxes in the surface boundary layer; and κ_{iw} represents diffusion by internal wave breaking. Spurious numerical mixing also plays a role in models. In order to minimise this, we employ the second-order-moment scheme of *Prather* [1986], which produces low numerical equivalent-vertical diffusivities below 10^{-5} m^2 s^{-1} [*Hill et al.*, 2012].

Additional parameters that constitute the model setup are the Coriolis parameter f (1×10^{-4} rad s^{-1}), its meridional gradient β (1×10^{-11} rad m^{-1} s^{-1}) and the thermal expansion coefficient α (2.4×10^{-4} °C^{-1}). Further details of our model setup can be obtained by downloading our model configuration, which can be obtained from the MITgcm CVS repository (see the acknowledgement section for details).

A control run is conducted with a realistic maximum wind stress, $\tau_0 = 0.1$ N m^{-2}, and no vertical mixing by internal wave breaking, $\kappa_{\mathrm{iw}} = 0$. The model is spun up for 200 years to achieve statistical equilibrium, and the last 10 years of this run are analysed. Five additional experiments are presented here in which vertical mixing associated with the generation and breaking of internal lee waves is represented by κ_{iw}. This representation is introduced at the end of year 100 of the control simulation, the model run for a further 100 years, and the last 10 years considered for analysis.

Five additional experiments are designed to assess the effects of small-scale topography and wind stress on the modelled circulation. Three of those simulations maintain the same wind forcing as the control run, and represent lee wave-induced diapycnal mixing with three different choices of the rms topographic height, h_{rms}, the primary topographic parameter affecting G and κ_{iw}. Spatially uniform h_{rms} values of 50 m, 150 m and 300 m are used, respectively corresponding to relatively smooth, moderate and abrupt topography in the Southern Ocean [*Scott et al.*, 2011]. The two final simulations adopt $h_{\mathrm{rms}} = 150$ m, and decrease or increase τ_0 by 50% (i.e. 0.05 N m^{-2}) with respect to other runs. In all perturbation experiments, the model solves equation (12) online at each grid point and time step, and the resulting κ_{iw} field both influences and is influenced by the circulation, allowing feedbacks to develop and a mutually consistent equilibrium to be attained. Note that the zonal volume transport integrated

across the channel varies minimally (by less than 5%) between experiments, and that eddy kinetic energy is insensitive to the prescribed h_{rms} yet reactive to variations in wind stress (the volume integral of eddy kinetic energy in the channel decreases or increases by 31% in the experiment with stronger or weaker winds, respectively). The insensitivity of zonal volume transport and responsiveness of eddy kinetic energy to changes in wind forcing in our model are in line with the 'eddy saturated' behaviour exhibited by the ACC in both observations and eddy-resolving simulations [see *Rintoul and Garabato*, 2013, and references therein].

4 Results

The circulation in the control run is illustrated by Figure 2. A snapshot of surface temperature and horizontal velocity (Fig. 2a) reveals the presence of an eastward jet flowing along the centre of the channel with peak speeds of ~ 0.5 m s^{-1}, roughly coincident with the maximum zonal wind stress and shedding eddies of both polarities measuring 30 - 100 km across. Meridional sections of the zonal- and time-mean potential temperature (Fig. 2b) and zonal velocity (Fig. 2c) indicate that the eastward jet is a permanent circulation feature, that it has an equivalent barotropic structure, and that it is in geostrophic balance with southward-shoaling isotherms. The zonal bottom velocities in the model peak at around around $9cms^{-1}$. In the ACC, bottom geostrophic flows as large as O(10)cms^{-1} have been found [*Polzin and Firing*, 1997; *Naveira Garabato et al.*, 2003], which compare well to our model results. Temperature classes colder than 0°C outcrop solely in a narrow region near the channel's southern boundary, yet dominate the deep interior, which is weakly stratified ($N \approx 3\times10^{-4}$ rad s^{-1}) compared to the uppermost ~ 1000 m. Note that this abyssal stratification is somewhat smaller than the typical values $\approx 10^{-3}$ rad s^{-1} observed on the abyssal Southern Ocean [e.g. *Scott et al.*, 2011]. Zonal-mean eddy kinetic energy (Fig. 2d) peaks at ~ 0.07 m^2 s^{-1} at the surface near the channel's axis and decays with depth by one to two orders of magnitude. The Eulerian-mean flow shows a classical Deacon Cell with meridional flow restricted to a northward near-surface wind-driven Ekman drift and a frictional near-bottom southward return flow. All of these properties of the modelled flow are quantitatively similar to those of ACC jets in observations [e.g. *Meijers et al.*, 2011] and eddy-resolving general circulation models [e.g. *Thompson and Naveira Garabato*, 2014], suggesting that our simulation is in a broadly realistic parameter regime.

The residual overturning streamfunction of our model simulations is calculated as the total time-averaged meridional flow below density (here reducing to temperature, as salinity

is constant) surfaces, remapped to the zonal-temporal mean depth of those surfaces, following *McDougall and McIntosh* [2001] and in particular *Nurser and Lee* [2004] (NL04). Thus the time-averaged meridional transport of fluid with temperature colder than a given θ_a across a given latitude y is:

$$\tilde{\psi}(y,\theta_a) = \left\langle \iint_{(x,z):\,\theta(x,y,z,t)\le\theta_a} -v\; dx\, dz \right\rangle, \tag{14}$$

(here we differ from NL04 and use the standard sign convention where the meridional streamfunction decreases upwards for northwards flow) indicating time averaging by the angled brackets $\langle\rangle$. The time-mean meridional isopycnal streamfunction $\tilde{\psi}(y,\theta_a)$ may be written as a function of y and z by identifying θ_a with its time-zonal-mean height

$$\tilde{z}(y,\theta_a) = \left\langle \frac{1}{L}\int_0^L z(y,\theta_a,t)\; dx \right\rangle \tag{15}$$

at each value of y, i.e. by writing

$$\tilde{\psi}(y,\theta_a) = \tilde{\Psi}(y,\tilde{z}(y,\theta_a)), \tag{16}$$

or equivalently,

$$\tilde{\Psi}(y,z) = \tilde{\psi}(y,\tilde{\theta}(y,z)), \tag{17}$$

where $\tilde{\theta}(y,z)$ is the temperature whose zonal-temporal average height is z at latitude y. Note that this $\tilde{\theta}(y,z)$ is different to the normal Eulerian-mean $\bar{\theta}(y,z)$, most markedly near the surface where $\tilde{\theta}(y,0)$ represents the *warmest* surface temperature that ever occurs at latitude y, not the *average* surface temperature, and similarly near the bottom $z=-H$ where $\tilde{\theta}(y,-H)$ represents the *coldest* bottom temperature that ever occurs at latitude y.

In the absence of drift (which is very small in our model runs over the averaging periods we choose), this stream-function can be related to the zonally-temporally averaged thickness weighted heating term

$$\tilde{Q}(y,z) = \lim_{\Delta\tilde{\theta}\to 0} \frac{\left\langle \iint_{(x,z):\,\tilde{\theta}\le\theta(x,y,z,t)\le\tilde{\theta}+\Delta\theta} \frac{D\theta}{Dt}\; dx\, dz \right\rangle}{\left\langle \iint_{(x,z):\,\tilde{\theta}\le\theta(x,y,z,t)\le\tilde{\theta}+\Delta\theta} dx\, dz \right\rangle} \tag{18}$$

according to

$$\frac{1}{L}\frac{\partial\tilde{\Psi}}{\partial y}\frac{\partial\tilde{\theta}}{\partial z} - \frac{1}{L}\frac{\partial\tilde{\Psi}}{\partial z}\frac{\partial\tilde{\theta}}{\partial y} = \tilde{Q}. \tag{19}$$

Here the y and z derivatives $\partial/\partial y$ and $\partial/\partial z$ are straightforward, taken at constant z and x respectively. The diabatic heating terms $\frac{D\theta}{Dt}$ include surface heating and cooling, relaxation forcing, the vertical diffusion D_v from (13), numerical diffusion $D_{\rm num}$ and the GM terms.

The time-averaged residual-mean circulation $\tilde{\Psi}$ in the control run exhibits a double overturning cell (Fig. 2e). The channel's interior is dominated by an anticlockwise lower cell, in which $\sim$ 3 Sv of the coldest temperature classes sink near the southern edge of the model domain, flow equatorward, and are ultimately returned upward and poleward. Note that our channel is only 1000 km long, so this transport would be very large if scaled up over the whole 18000 km length of the ACC; this results from our strong cooling that does not occur in reality all around the ACC. A weaker (~ 0.5 Sv) clockwise upper cell is also present in the northern half of the channel. The bulk of the diathermal flow in both cells occurs in the diabatic surface layer (DSL, defined as the layer above the time-mean depth of the coldest isothermal that has entered the surface mixed layer in the period over which the circulation is temporally averaged, and indicated by the thick black line in Figure 2e), which is directly forced by the surface heat flux, and near the segment of the northern boundary sponge layer encompassed by the upper cell. Consistent with the weak interior vertical mixing prescribed in the control run, residual flow below the DSL is largely directed along isotherms. Note that the bottom (densest) residual-mean flow is northward, while the Eulerian-mean flow is everywhere southward. The structure of the simulated residual-mean circulation qualitatively resembles that of the Southern Ocean overturning, although there are significant quantitative differences between the two after the modelled circulation is scaled to the zonal extent of the Southern Ocean. Unlike in the model's case, the two Southern Ocean overturning cells are of comparable magnitude, with the upper (lower) cell being stronger (weaker) than its simulated counterpart by approximately a factor of 2 [e.g. *Garabato et al.*, 2014]. These differences are, however, of little consequence to our study, which focusses on the character and *relative* magnitude of the AABW-like lower cell's response to lee wave-induced diapycnal mixing.

We next consider the simulations with parameterised lee wave-induced diapycnal mixing. The key results for all experiments are summarized in Table 1. First, we note that the channel-averaged energy transferred to the lee wave field varies from 0.07 mW m^{-2} for the experiment with low h_{rms} (50 m), to 0.13 mW m^{-2} with moderate (150 m) and 0.18 mW m^{-2} with high (300 m) values of h_{rms}; for the experiments with $h_{\mathrm{rms}} = 150$ m and stronger and weaker winds, lee wave energy radiation is 0.20 mW m^{-2} and 0.04 mW m^{-2}, respectively. The increase in lee wave energy transfer with h_{rms} is much less notable than the quadratic increase ($\propto h_{\mathrm{rms}}^2$) expected from (7); this results from an almost linear dependence of lee wave energy radiation on near-bottom stratification (which of course vanishes at $N = f \approx 10^{-4}$ rad s^{-1}) together with the reduction in stratification (see below) driven by the intensified near-

bottom mixing. Since the bottom stratification in these runs is so weak, the IW drag coefficient given by the theory of section 2.1, is in fact an order of magnitude less than than the large value of bottom drag $C_d = 0.01$ applied in our model runs.

The effect of the inclusion of lee wave-induced diapycnal mixing on the modelled diapycnal diffusivity and stratification is synthesised for the three perturbation experiments with low (50 m), moderate (150 m) and high (300 m) values of h_{rms} (Fig. 3d). The horizontally and temporally averaged profiles of κ reveal an intensification of diapycnal mixing relative to the control run in all three experiments that is more pronounced with increasing h_{rms}, with mean values of 3.14×10^{-4} m^2 s^{-1} ($h_{\mathrm{rms}} = 50$ m), 9.52×10^{-4} m^2 s^{-1} ($h_{\mathrm{rms}} = 150$ m) and 1.39×10^{-3} m^2 s^{-1} ($h_{\mathrm{rms}} = 300$ m) in the bottom 1000 m (Fig. 3d). The enhancement of κ has a significant impact on the modelled stratification, which is reduced as h_{rms} increases (Fig. 3d). This reduction is associated with a widespread warming of the Eulerian-temporal-mean temperature in the channel interior and the southern reaches of the DSL, and with a cooling of the upper levels near the northern edge of the domain (Fig. 3a–c). The warming has two maxima: one near the bottom, where the change in κ is largest; and another in the warmest temperature classes implicated in the lower cell, which shoal from depths of 500–1400 m at the northern boundary to the surface near the southern boundary.

The elevation of diapycnal mixing and weakening of stratification with increasing h_{rms} induce a substantial response in the residual-mean circulation (Fig. 4). With rougher topography, the lower overturning cell intensifies and is progressively focussed closer to the bottom, as evidenced by the dipole pattern in the residual-mean streamfunction anomaly. Away from the DSL, the axis of the dipole is close to a depth of 2000 m, below which lee wave-induced diapycnal mixing is confined. The upper overturning cell is essentially unchanged in all perturbation experiments. Panels 4d–f show the increased zonally-averaged heating rate relative to the control for the three runs (again calculated on isotherms and remapped to their zonal-temporal-mean height), diagnosed from the residual mean temperature equation (19); the near-bottom warming and compensating cooling over the deepest 1000 m predicted by (10) are evident. Note that in the abyssal cell, warming happens first as the bottom waters drift northward and the water is cooled afterwards as the waters drift southward and upwards, so, as seen in (Fig. 3a–c) the water is everywhere warmer than before despite the mid-depth cooling (though the temperature increase is greatest near the bottom).

An overview of how the temperature and transport of the lower overturning cell vary with h_{rms} is given by Figure 5a, in which average values of the zonal-mean temperature and the residual-mean streamfunction over an area spanning the bottom 1000 m of the channel away from the DSL (the red box in Figure 2e) are displayed as functions of topographic roughness. Both the temperature and strength of the lower cell increase monotonically with growing h_{rms}, although at rates that decrease with increasing roughness. This behaviour is related to the relative change in κ, which increases approximately 30-fold between the control simulation and the experiment with $h_{\mathrm{rms}} = 50$ m, but only by a further factor of 1.5–3.0 for runs with higher roughness. The changes in the temperature and transport of the lower cell in the perturbation runs are significant, amounting to up to approximately 70% of the temperature difference between the down- and upwelling limbs of the cell and of the cell's transport in the control simulation.

The outcome of the experiments with $h_{\mathrm{rms}} = 150$ m and perturbed eastward wind stress is synthesised by Figure 5b. A reduction (increase) of 50% in the maximum eastward wind stress leads to a substantial warming (cooling) and weakening (strengthening) of the lower overturning cell. The response is of comparable magnitude to that in the experiments with perturbed topographic roughness, and is more pronounced for a reduction than for an increase in wind stress.

Finally, the dependency of the diapyncal diffusivity on the wind stress for the experiments with $h_{\mathrm{rms}} = 150$ m is shown in Figure 5c. The response of the diffusivity to 50% weaker wind stress is approximately comparable to the result obtained by decreasing h_{rms} to 50m, which reduces the near-bottom diffusivity by about 5×10^{-4} m^2 s^{-1}. Increasing the wind stress by 50% yields a less intense response in the diffusivity with an increase of about 8×10^{-4} m^2 s^{-1} which is very similar to the result obtained by increasing h_{rms} to 300m.

5 Discussion

The set of model experiments presented above indicates (i) that the transport and temperature (density) of deep meridional overturning across an ACC-like, eddying zonal flow is significantly controlled by lee wave-induced diapycnal mixing linked to the (parameterized) interaction of mesoscale eddies with small-scale topography; and (ii) that this mechanism brings about a significant sensitivity of the deep residual meridional overturning to wind forcing per-

turbations. These findings qualitatively endorse our starting hypothesis. Next, we consider the physics underpinning the quantitative aspects of the modelled overturning behaviour.

In the steady state, the variation of $\tilde{\Psi}$ with y on an isotherm of constant $\tilde{\theta}$ is given by the elegant expression, which comes immediately [*Ito and Marshall*, 2008] from re-arranging (19) to yield

$$\left.\frac{\partial\tilde{\Psi}}{\partial y}\right|_{\tilde{\theta}} = -\tilde{Q}\left(\frac{\partial\tilde{\theta}}{\partial z}\right)^{-1}. \tag{20}$$

Ito and Marshall then integrated (20) from some value of y to the value $y_{\mathrm{bottom}}(\tilde{\theta})$ where the isotherm strikes the bottom and the streamfunction $\tilde{\Psi} = 0$; they assumed (i) a constant vertical diffusivity and (ii) a stratification decaying exponentially with scale depth D to give their Eq. (11):

$$\tilde{\Psi}(y,\tilde{\theta}) = \frac{\kappa}{D}(y - y_{\mathrm{bottom}}(\tilde{\theta})). \tag{21}$$

This simple relation (21) describes a balance between deep-ocean buoyancy loss by advection across the isotherm and buoyancy gain by diapycnal mixing. Its direct use to diagnose our model runs would suggest much stronger abyssal cells in the runs with lee-wave forcing than in the control run, given (Table 1) that the deep diffusivities over the bottom 1000 m are stronger than that in the control run by 28 $\times$ in the lee-waves forced with $h_{\mathrm{rms}} = 50\,\mathrm{m}$, 87 $\times$ with $h_{\mathrm{rms}} = 150\,\mathrm{m}$ and 126 $\times$ greater with $h_{\mathrm{rms}} = 300\,\mathrm{m}$. Clearly the increases in the overturning circulation that we see are proportionately far weaker e.g. at $2500\,\mathrm{m}$ depth in the southern half of the channel, the control $\tilde{\Psi}$ is $\approx -2\,\mathrm{Sv}$, increasing in strength to $\approx -2.7\,\mathrm{Sv}$ with $h_{\mathrm{rms}} = 50\,\mathrm{m}$, to $\approx -3.2\,\mathrm{Sv}$ with $h_{\mathrm{rms}} = 150\,\mathrm{m}$ and to $\approx -3.4\,\mathrm{Sv}$ with $h_{\mathrm{rms}} = 150\,\mathrm{m}$. So why is this response so much weaker?

Most importantly (10), the downward buoyancy flux driven by the breaking lee-waves attains a maximum just above the bottom boundary, and then reduces upwards following the prescribed linear $F(z)$, implying an intense δ-function buoyancy (heat) gain along the bottom boundary but constant buoyancy *loss* (cooling) throughout the rest of the modelled deep ocean. This is consistent with a recent study by *de Lavergne et al.* [2015], who find that the bottommost waters in the Southern Ocean gain buoyancy in the presence of near-bottom mixing whereas the overlying waters experience a buoyancy loss. This pattern of strong near bottom warming and compensating cooling over the bottom $1000\,\mathrm{m}$ implies by (20) a rapid decrease of $\tilde{\Psi}$ from zero just south of the grounding latitude y_{bottom} (where the isotherm lies in the region of bottom warming), followed by a gradual return towards zero over the isotherm trajectory as it slopes upwards through the bottom $1000\,\mathrm{m}$—this gives very different dependence of $\tilde{\Psi}$

on y to that predicted by the simple relation (21). This pattern of decreasing and then increasing streamfunction along the isotherms as they curve southwards and upwards (e.g. Fig. 2a) is consistent with the counter-clockwise perturbation cells confined to the bottom $1000\,\mathrm{m}$ evident in Fig. 4a–c. Near-bottom buoyancy gain drives northward flow across the sloping isotherms, balanced by southward flow across shallower isotherms driven by buoyancy loss. Because of the oppositely signed, cancellatory, contributions to the streamfunction the strength of the response is far weaker than would be predicted by the simple estimate (21) for consistent buoyancy gain (warming).

However this argument does not of itself explain why the anomalous bottom cell strength does not then scale with the increasing κ_{iw} with h_{rms}. For instance κ_{iw} increases almost by a factor of three as h_{rms} increases from $50\,\mathrm{to}\,150\,\mathrm{m}$, but the anomalous $\tilde{\Psi}$ strengthens only by a factor of $\sim$1.4. And (20) suggests that it should be the diabatic heating divided by the stratification that sets $\frac{\partial\tilde{\Psi}}{\partial y}\Big|_{\tilde{\theta}}$; since the diabatic heating/cooling is proportional to the lee-wave driven buoyancy flux, it is proportional to κ_{iw} after division by the stratification. One explanation for this is that although the vertical buoyancy (temperature) gradient weakens, the *horizontal* buoyancy (temperature) gradient changes little with h_{rms}. In terms of (20), this means that isotherms are almost twice as steep with $h_{\mathrm{rms}} = 150\,\mathrm{m}$ (mean bottom $N{\approx}1.6\times10^{-4}\,\mathrm{rad}^{-1}$) than with $h_{\mathrm{rms}} = 50\,\mathrm{m}$ (mean bottom $N{\approx}2\times10^{-4}\,\mathrm{rad}^{-1}$). Hence, although $\partial\tilde{\Psi}/\partial y\Big|_{\tilde{\theta}}$ increases by a factor of three, the horizontal distance moved as the isotherm moves upwards through the bottom $1000\,\mathrm{m}$ reduces almost by a factor of two, so $\tilde{\Psi}$ only changes by a factor of $\approx$1.7. The importance of the horizontal buoyancy gradients is also evident from direct comparison of the contributions of the $\partial\tilde{\Psi}/\partial y{\cdot}\partial\tilde{\theta}/\partial z$ and $-\partial\tilde{\Psi}/\partial z{\cdot}\partial\tilde{\theta}/\partial y$ terms to the buoyancy (heat) budget in (19).

Indeed, no circulation would develop in our scenario of a flat-bottomed ocean with lee-wave mixing without the lateral advection, as bottom waters would simply warm and convectively mix with the cooling deep waters in the bottom$1000\,\mathrm{m}$. Although in reality the vertical stratification is considerably greater than in our model, our conclusion that lateral advection should make an important contribution to the density budget is, we believe, robust; isopycnal slopes in the abyssal Southern Ocean can easily reach 10^{-3} [*Rintoul and Garabato*, 2013], similar to the values in our model. Our findings here agree with those of *Mashayek et al.* [2015], who emphasize the importance of horizontal advection in the closure of the mixing driven overturning circulation.

Another process which has a major impact on the lower-cell overturning driven by lee wave-induced diapycnal mixing in our simulations is the variance in the depth of the isopycnals associated with the actively eddying pseudo-ACC. Now, at any one time, the lee wave-induced buoyancy flux, gives a δ-function buoyancy (heat) gain near the bottom, balanced by uniform buoyancy loss $B_{\rm iw0}$ (cooling) throughout the deepest 1000 m. In the discretized numerical model, the deep (>1500 m depth) grid boxes have uniform thickness, 101.5 m, and the δ-function buoyancy forcing at the bottom grid level reduces to $9|B_{\rm iw0}|$. This pattern of buoyancy forcing may be expected to drive an overturning cell with northward flow and diapycnal upwelling in a thin boundary layer adjacent to the bottom boundary, and southward flow and diapycnal downwelling elsewhere in the deepest kilometre. However, the mesoscale eddies in our simulation displace isotherms vertically, leading to a relatively wide range of isotherms being in occasional contact with the bottom boundary. Over time, this results in a spreading of the near-bottom buoyancy gain into lighter isopycnals, which appears in the residual mean view as an 'upward' spreading and broadens the time-mean vertical extent of the northward-flowing layer. This effect, in which a range of isopycnals (isotherms) come into contact with the relatively strongly forced bottom layer is directly analogous to the diabatic surface layer (DSL) where a wide range of isopycnals—all those lighter than the densest isopycnal that ever outcrops into the surface mixed-layer—may be exposed to surface forcing.

To illustrate this effect of mesoscale eddies, in Figure 6a each colored line represents a given 100m-thick range (specified by the line color), and the dots on the line represent the percentage of time that this depth range is occupied by isopycnals (isotherms) with mean depths in different 100-m ranges centred at the depths of the dots. This is along a specific zonal line, halfway across the channel (800km north of the southern side), for the full 10-year analysis period in the simulation with $h_{\rm rms} = 300$ m. The bottom boundary influence is found to extend upward 300–400 m, in line with the vertical scale of the northward limb of lower-cell overturning (Figure 4a–c) and diagnosed IW forcing (Fig. 4d–f). An overview of how the vertical extent of this bottom boundary influence changes across our suite of experiments, i.e. the vertical structure of the $\tilde{Q}$ produced by the internal waves, is provided by Figure 6b. As explained above, without any isothermal movement the scaled buoyancy input would be 9 in the bottom gridbox, and -1 up to a depth of -2000 m. The upward spreading is greatest for the simulations with the roughest topography and strongest wind forcing, and most modest for the runs with the least rough topography and weakest wind forcing. This follows the weaker (stronger) stratification/more (less) energetic eddies in the former (latter) simulations, which yields el-

evated (reduced) vertical displacements of isotherms. We suggest that the role of mesoscale eddies in propagating the near-bottom buoyancy gain upward over a substantial vertical scale is likely to be a realistic feature of our simulations, as it is founded on robust aspects of the modelled physics: the enhancement of diapycnal buoyancy fluxes toward the seafloor over rough topography [*Waterman et al.*, 2013; *Sheen et al.*, 2013]; the induction by eddies of vertical displacements of isopycnals of O(100 m) [*Thompson and Naveira Garabato*, 2014]; and the sensitivity of eddy kinetic energy to wind forcing [*Meredith et al.*, 2012].

6 Conclusions

The hypothesis that the eddy field's impingement on small-scale topography may regulate diapycnal mixing and meridional overturning across the deep Southern Ocean has been assessed in an idealised model. The model simulates an eddying circumpolar current coupled to a double-celled meridional overturning with properties broadly resembling those of the Southern Ocean circulation, and represents lee wave-induced diapycnal mixing using an online formulation grounded on wave radiation theory. We show that the lee wave-induced diapycnal mixing generated by the simulated eddy field plays a major role in sustaining the lower overturning cell in the model, and that it underpins a significant sensitivity of this cell to wind forcing perturbations. While some simulated aspects of the overturning's quantitative dependence on diapycnal mixing are likely to be model-specific, our simulations suggest that the Southern Ocean lies in a parameter regime where lee waves may be of dynamical importance to meridional overturning, and point to a role of mesoscale eddies in vertically propagating the effects of enhanced near-bottom diapycnal mixing.

Our suggestion that lee wave-induced diapycnal mixing plays a significant role in sustaining deep Southern Ocean overturning resonates with the findings of several recent studies based on offline applications of wave radiation theory [*Nikurashin and Ferrari*, 2013; *Stanley and Saenko*, 2014; *Mélet et al.*, 2014]. The online formulation in our model allows us to extend these findings by unveiling how mesoscale eddies both underpin the response of deep diapycnal mixing and meridional overturning to wind forcing, and set the vertical structure of that response. Motivated by the recent and projected interdecadal intensification of the Southern Hemisphere westerlies [*Thompson and Richards*, 2011], many authors have investigated the eddy-mediated sensitivity of the upper cell of Southern Ocean overturning to atmospheric forcing perturbations [see e.g. *Meredith et al.*, 2012, and references therein], and suggested that flow–topography interactions are important in understanding that sensitivity [see *Rintoul and*

Garabato, 2013, and references therein]. Our results indicate that the lower cell of Southern Ocean overturning is likely to respond to wind forcing too, via a distinct form of flow–topography interaction involving the generation and breaking of lee waves.

Like most idealised studies, ours suffers from several simplifications that may either exaggerate or understate the significance of lee wave radiation and breaking in shaping meridional overturning across the deep Southern Ocean. We have not included the effect of the IW drag on the deep flows, though we know that it is important in realistic parameter regimes [*Naveira Garabato et al.*, 2013]. Also, the circulation of newly formed bottom waters in the Southern Ocean is strongly influenced by diapycnal mixing in downslope flows and topographically guided deep boundary currents, which is likely regulated by processes distinct from lee wave radiation [e.g. *Polzin et al.*, 2014]. Further, the theory upon which our formulation of lee wave-induced diapycnal mixing is based has been suggested to significantly overestimate microstructure-derived values of κ [*Waterman et al.*, 2013; *Sheen et al.*, 2013], likely in connection with three-dimensional, finite-amplitude topographic effects [*Nikurashin et al.*, 2014]. On the other hand, the deep stratification in our model is considerably weaker than in the Southern Ocean, which significantly reduces the efficiency of energy transfer to the lee wave field. Despite these caveats, our work indicates that the Southern Ocean lies in a parameter regime where lee waves may be of dynamical importance to meridional overturning and, in revealing complex feedbacks between deep eddy flows, lee wave generation and overturning, highlights the requirement of representing lee wave processes online. Determining the degree to which our findings hold in the ocean will entail the extension of our approach to realistic general circulation models, and the precise assessment of lee wave parameterizations with observations.

Acknowledgments

MBB was supported by the U.K. Natural Environment Research Council (NERC) via a Ph.D. scholarship awarded as part of the SOFine project (NE/G001510/1). We thank David Ferreira, Maxim Nikurashin and Kurt Polzin for helpful discussions as well as the editor and two anonymous reviewers for their constructive comments. The online internal wave code and any additional code that is required to run the model is available from George Nurser (g.nurser@noc.ac.uk).

References

Abernathey, R., J. Marshall, and D. Ferreira (2011), The dependence of Southern Ocean meridional overturning on wind stress, *Journal of Physical Oceanography*, *41*(12),

2261–2278.

Bell, T. H. (1975), Lee waves in stratified flows with simple harmonic time dependence, *Journal of Fluid Mechanics*, *67*(04), 705–722.

Brearley, J. A., K. L. Sheen, A. C. Naveira Garabato, D. A. Smeed, and S. Waterman (2013), Eddy-induced modulation of turbulent dissipation over rough topography in the Southern Ocean, *Journal of Physical Oceanography*, *43*(11), 2288–2308, doi: 10.1175/JPO-D-12-0222.1.

de Lavergne, C., G. Madec, J. Le Sommer, A. J. G. Nurser and A. C. Naveira Garabato (2015), On the consumption of Antarctic Bottom Water in the abyssal ocean, *Journal of Physical Oceanography*, *46*(2), 635–661,doi:10.1175/JPO-D-14-0201.1.

Dufour, C. O., J. Le Sommer, J. D. Zika, M. Gehlen, J. C. Orr, P. Mathiot, and B. Barnier (2012), Standing and transient eddies in the response of the Southern Ocean meridional overturning to the southern annular mode, *Journal of Climate*, *25*(20), 6958–6974, doi:10.1175/JCLI-D-11-00309.1.

Ferrari, R., and M. Nikurashin (2010), Suppression of eddy diffusivity across jets in the Southern Ocean, *Journal of Physical Oceanography*, *40*(7), 1501–1519.

Garabato, A. C. N., A. P. Williams, and S. Bacon (2014), The three-dimensional overturning circulation of the Southern Ocean during the {WOCE} era, *Progress in Oceanography*, *120*, 41 – 78, doi:http://dx.doi.org/10.1016/j.pocean.2013.07.018.

Gent, P. R., and J. C. McWilliams (1990), Isopycnal mixing in ocean circulation models, *Journal of Physical Oceanography*, *20*(1), 150–155.

Gill, A. E. (1982), *Atmosphere-ocean dynamics*, vol. 30, Academic press.

Goff, J. A., and B. K. Arbic (2010), Global prediction of abyssal hill roughness statistics for use in ocean models from digital maps of paleo-spreading rate, paleo-ridge orientation, and sediment thickness, *Ocean Modelling*, *32*(1-2), 36 – 43.

Goff, J. A., and T. H. Jordan (1988), Stochastic modeling of seafloor morphology: Inversion of sea beam data for second-order statistics, *J. Geophys. Res.*, *93*(B11), 13,589–13,608.

Goff, J. A., and T. H. Jordan (1989), Stochastic modeling of seafloor morphology: A parameterized gaussian model, *Geophys. Res. Lett.*, *16*(1), 45–48.

Griffies, S. M. (1998), The Gent–McWilliams skew flux, *Journal of Physical Oceanography*, *28*(5), 831–841.

Hallberg, R., and A. Gnanadesikan (2006), The role of eddies in determining the structure and response of the wind-driven southern hemisphere overturning: Results from the modeling eddies in the Southern Ocean (MESO) project, *Journal of Physical Oceanography*, *36*(12), 2232–2252.

Hill, C., D. Ferreira, J.-M. Campin, J. Marshall, R. Abernathey, and N. Barrier (2012), Controlling spurious diapycnal mixing in eddy-resolving height-coordinate ocean models – insights from virtual deliberate tracer release experiments, *Ocean Modelling*, *45–46*(0), 14–26.

Ito, T., and J. Marshall (2008), Control of lower limb circulation in the Southern Ocean by diapycnal mixing and mesoscale eddy transfer, *Journal of Physical Oceanography*, *38*(12), 2832–2845.

Large, W. G., J. C. McWilliams, and S. C. Doney (1994), Oceanic vertical mixing: A review and a model with a nonlocal boundary layer parameterization, *Rev. Geophys.*, *32*(4), 363–403.

Marshall, J., and T. Radko (2003), Residual-mean solutions for the Antarctic Circumpolar Current and its associated overturning circulation, *Journal of Physical Oceanography*, *46*(11), 2341–2354.

Marshall, J., and K. Speer (2012), Closure of the meridional overturning circulation through Southern Ocean upwelling, *Nature Geoscience*, *5*(3), 171–180.

Marshall, J., C. Hill, L. Perelman, and A. Adcroft (1997a), Hydrostatic, quasi-hydrostatic, and nonhydrostatic ocean modeling, *J. Geophys. Res.*, *102*(C3), 5733–5752.

Marshall, J., A. Adcroft, C. Hill, L. Perelman, and C. Heisey (1997b), A finite-volume, incompressible Navier Stokes model for studies of the ocean on parallel computers, *J. Geophys. Res.*, *102*(C3), 5753–5766.

Mashayek, A., R. Ferrari, M. Nikurashin and W. R. Peltier (2015), Full Access Influence of Enhanced Abyssal Diapycnal Mixing on Stratification and the Ocean Overturning Circulation, *Journal of Physical Oceanography*, *45*(10), 2580–2597.

McDougall, T. J., and P. C. McIntosh (2001), The temporal-residual-mean velocity. part ii: Isopycnal interpretation and the tracer and momentum equations, *Journal of Physical Oceanography*, *31*(5), 1222–1246, doi:10.1175/1520-0485(2001)031¡1222:TTRMVP¿2.0.CO;2.

Meijers, A. J. S., N. L. Bindoff, and S. R. Rintoul (2011), Estimating the four-dimensional structure of the Southern Ocean using satellite altimetry, *Journal of Atmospheric and*

Oceanic Technology, *28*(4), 548–568, doi:10.1175/2010JTECHO790.1.

Mélet, A., R. Hallberg, S. Legg, and M. Nikurashin (2014), Sensitivity of the ocean state to lee wave–driven mixing, *Journal of Physical Oceanography*, *44*(3), 900–921, doi: 10.1175/JPO-D-13-072.1.

Meredith, M. P., A. C. Naveira Garabato, A. M. Hogg, and R. Farneti (2012), Sensitivity of the overturning circulation in the Southern Ocean to decadal changes in wind forcing, *Journal of Climate*, *25*(1), 99–110, doi:10.1175/2011JCLI4204.1.

Morrison, A. K., and A. McC. Hogg (2013), On the relationship between Southern Ocean overturning and ACC transport, *Journal of Physical Oceanography*, *43*(1), 140–148, doi:10.1175/JPO-D-12-057.1.

Munk, W., and C. Wunsch (1998), Abyssal recipes II: Energetics of tidal and wind mixing, *Deep Sea Research Part I: Oceanographic Research Papers*, *45*(12), 1977–2010.

Naveira Garabato, A. C., D. P. Stevens and K. J. Heywood (2003), Water mass conversion, fluxes and mixing in the Scotia Sea diagnosed by an inverse model, *Journal of Physical Oceanography*, *33*(12), 2565–2587.

Naveira Garabato, A. C., K. L. Polzin, B. A. King, K. J. Heywood, and M. Visbeck (2004), Widespread intense turbulent mixing in the Southern Ocean, *Science*, *303*(5655), 210–213.

Naveira Garabato, A. C., A. J. G. Nurser, R. B. Scott, and J. A. Goff (2013), The impact of small-scale topography on the dynamical balance of the ocean, *Journal of Physical Oceanography*, *43*(3), 647–668, doi:10.1175/JPO-D-12-056.1.

Nikurashin, M., and R. Ferrari (2010a), Radiation and dissipation of internal waves generated by geostrophic motions impinging on small-scale topography: Theory, *Journal of Physical Oceanography*, *40*(5), 1055–1074.

Nikurashin, M., and R. Ferrari (2010b), Radiation and dissipation of internal waves generated by geostrophic motions impinging on small-scale topography: Application to the Southern Ocean, *Journal of Physical Oceanography*, *40*(9), 2025–2042.

Nikurashin, M., and R. Ferrari (2013), Overturning circulation driven by breaking internal waves in the deep ocean, *Geophysical Research Letters*, *40*(12), 3133–3137, doi:10.1002/grl.50542.

Nikurashin, M., and G. Vallis (2011), A theory of deep stratification and overturning circulation in the ocean, *Journal of Physical Oceanography*, *41*(3), 485–502.

Nikurashin, M., R. Ferrari, N. Grisouard, and K. Polzin (2014), The impact of finite-amplitude bottom topography on internal wave generation in the Southern Ocean, *Journal of Physical Oceanography*, *44*(11), 2938–2950, doi:10.1175/JPO-D-13-0201.1.

Nurser, A. J. G., and M.-M. Lee (2004), Isopycnal averaging at constant height. part ii: Relating to the residual streamfunction in Eulerian space, *Journal of Physical Oceanography*, *34*(12), 2740–2755, doi:10.1175/JPO2650.1.

Olbers, D., D. Borowski, C. Völker, and J. Wolff (2004), The dynamical balance, transport and circulation of the Antarctic Circumpolar Current, *Antarctic Science*, *16*(4), 439–470.

Osborn, T. R. (1980), Estimates of the local rate of vertical diffusion from dissipation measurements, *Journal of Physical Oceanography*, *10*(1), 83–89.

Osborn, T. R., and C. S. Cox (1972), Oceanic fine structure, *Geophysical Fluid Dynamics*, *3*(1), 321–345, doi:10.1080/03091927208236085.

Polzin, K. L., and E. Firing (1997), An abyssal recipe, *Ocean Modelling*, *30*(4), 298 – 309.

Polzin, K. L. (2009), Estimates of Diapycnal Mixing Using LADCP and CTD data from I8S, *WOCE International Newsletter*, *29*, 29 – 42.

Polzin, K. L., A. C. N. Garabato, E. P. Abrahamsen, L. Jullion, and M. P. Meredith (2014), Boundary mixing in Orkney Passage outflow, *Journal of Geophysical Research: Oceans*, *119*(12), 8627–8645, doi:10.1002/2014JC010099.

Prather, M. J. (1986), Numerical advection by conservation of second-order moments, *J. Geophys. Res.*, *91*(D6), 6671–6681.

Rintoul, S. R., and A. C. N. Garabato (2013), Chapter 18 - dynamics of the Southern Ocean circulation, in *Ocean Circulation and ClimateA 21st Century Perspective*, *International Geophysics*, vol. 103, edited by J. G. Gerold Siedler, Stephen M. Griffies and J. A. Church, pp. 471 – 492, Academic Press, doi:http://dx.doi.org/10.1016/B978-0-12-391851-2.00018-0.

Scott, R. B., J. A. Goff, A. C. Naveira Garabato, and A. J. G. Nurser (2011), Global rate and spectral characteristics of internal gravity wave generation by geostrophic flow over topography, *J. Geophys. Res.*, *116*(C9).

Sheen, K., A. N. Garabato, J. Brearley, M. Meredith, K. Polzin, D. Smeed, A. Forryan, B. King, J.-B. Sallée, L. S. Laurent, et al. (2014), Eddy-induced variability in Southern Ocean abyssal mixing on climatic timescales, *Nature Geoscience*.

Sheen, K. L., J. A. Brearley, A. C. Naveira Garabato, D. A. Smeed, S. Waterman, J. R. Ledwell, M. P. Meredith, L. St. Laurent, A. M. Thurnherr, J. M. Toole, and A. J. Watson (2013), Rates and mechanisms of turbulent dissipation and mixing in the Southern Ocean: Results from the diapycnal and isopycnal mixing experiment in the Southern Ocean (DIMES), *Journal of Geophysical Research: Oceans*, *118*(6), 2774–2792, doi: 10.1002/jgrc.20217.

Speer, K., S. R. Rintoul, and B. Sloyan (2000), The diabatic Deacon Cell*, *Journal of Physical Oceanography*, *30*(12), 3212–3222.

St. Laurent, L., A. C. Naveira Garabato, J. R. Ledwell, A. M. Thurnherr, J. M. Toole, and A. J. Watson (2012), Turbulence and diapycnal mixing in Drake Passage, *Journal of Physical Oceanography*, *42*(12), 2143–2152, doi:10.1175/JPO-D-12-027.1.

St. Laurent, L. C., H. L. Simmons, and S. R. Jayne (2002), Estimating tidally driven mixing in the deep ocean, *Geophysical Research Letters*, *29*(23), 21.1–21.4.

Stanley, G. J., and O. A. Saenko (2014), Bottom-enhanced diapycnal mixing driven by mesoscale eddies: Sensitivity to wind energy supply, *Journal of Physical Oceanography*, *44*(1), 68–85, doi:10.1175/JPO-D-13-0116.1.

Talley, L. (2013), Closure of the global overturning circulation through the Indian, Pacifc, and Southern Oceans: Schematics and transports., *Oceanography*, *26*(1), 80–97, doi: 10.5670/oceanog.2013.07.

Thompson, A. F., and A. C. Naveira Garabato (2014), Equilibration of the Antarctic Circumpolar Current by standing meanders, *Journal of Physical Oceanography*, *44*(7), 1811–1828, doi:10.1175/JPO-D-13-0163.1.

Thompson, A. F., and K. J. Richards (2011), Low frequency variability of Southern Ocean jets, *Journal of Geophysical Research: Oceans*, *116*(C9), n/a–n/a, doi: 10.1029/2010JC006749, c09022.

Waterman, S., A. C. Naveira Garabato, and K. L. Polzin (2013), Internal waves and turbulence in the Antarctic Circumpolar Current, *Journal of Physical Oceanography*, *43*(2), 259–282, doi:10.1175/JPO-D-11-0194.1.

Figure 1: A schematic illustration of the model domain and the main forcing mechanisms. The unshaded areas represent solid walls.

Figure 2: The control experiment: a) A snapshot and the time-mean distribution of the surface potential temperature (°C, colours) overlaid with horizontal velocities (m s^{-1}, vector arrows). Average zonal mean sections of: b) the potential temperature (°C), c) the zonal velocity (m s^{-1}), d) the average eddy kinetic energy (m^2 s^{-2}) and e) the residual overturning streamfunction (Sv). The thick black line in panel e) is the boundary of the diabatic surface forcing (DSF), as defined in the text and the red box denotes the area of averaging for the results in Fig. 5.

Table 1: A summary of the key results for all experiments. The ILW energy generation rate G is averaged over the whole channel, the mean residual overturning $\tilde{\Psi}$ and the mean potential temperature θ ave averaged over the area of the red box in Fig. 2e) and the mean diapycnal diffusivity κ over the bottom 1000 m.

h_{rms}	wind	mean G	mean κ	mean $\tilde{\Psi}$	mean θ
0 m	control	0 mW m^{-2}	1.00×10^{-5} m^2 s^{-1}	-0.89 Sv	-1.00 °C
50 m	control	0.07 mW m^{-2}	3.14×10^{-4} m^2 s^{-1}	-1.10 Sv	-0.97 °C
150 m	control	0.13 mW m^{-2}	9.52×10^{-4} m^2 s^{-1}	-1.34 Sv	-0.96 °C
300 m	control	0.18 mW m^{-2}	1.39×10^{-3} m^2 s^{-1}	-1.49 Sv	-0.95 °C
150 m	- 50%	0.04 mW m^{-2}	4.57×10^{-4} m^2 s^{-1}	-0.76 Sv	-0.83 °C
150 m	+ 50%	0.20 mW m^{-2}	1.33×10^{-3} m^2 s^{-1}	-1.54 Sv	-1.03 °C

Figure 3: Panels a), b) and c) show the average zonal mean section of the potential temperature difference (°C) between each experiment with increasing bottom roughness parameters h_{rms} and the control experiment for h_{rms}=50 m, 150 m and 300 m respectively. The thick black line denotes the DSF line. Panel d) shows the channel-mean average buoyancy frequency profiles (dashed) and diapycnal diffusivity profiles (solid) for all experiments.

Figure 4: a), b), c): The difference in the zonally integrated average residual-mean streamfunction (Sv) between the results from each experiment with increasing bottom roughness parameters h_{rms} and the control experiment. Panel a) shows the result for h_{rms}=50 m, b) for h_{rms}=150 m and c) for h_{rms}=300 m. The thick black line denotes the DSF line. Panels d), e) and f) show the differences between the residual-mean heating for the respective runs and in the control experiment in mdeg °C yr^{-1}. The heating is zonally-averaged and thickness-weighted on isotherms with given mean depth, calculated from the residual-mean streamfunction according to (**??**).

Figure 5: Summary of the evolution of the mean strength of the lower limb and the potential temperature with a) the bottom roughness parameter for h_{rms} and b) with the wind stress for h_{rms}=150m. The averaging was carried out over the area encompassed by the red box in Fig. 2e). For h_{rms}=150m the dependency of the diapycnal diffusivity on the wind stress is shown in c).

Figure 6: a). Each colored line represents a given 100m-thick range (specified by its color) and the dots on the line represent the percentage of time (at the middle of the channel, y = 800 km) that this range is occupied by isotherms with different mean depths (horizontal scale). So e.g. the leftmost (blue) line represents the % of time that the bottom 100 m is occupied by isotherms with mean depths -2950 ± 50 m, -2850 ± 50, ... For the run with h_{rms} = 300 m. b). Values of thickness weighted buoyancy input as functions of mean depth of the isotherm onto which the buoyancy input is projected (**??**), for the different runs, scaled by the theoretical interior buoyancy loss $|B_{\mathrm{iw0}}|$.

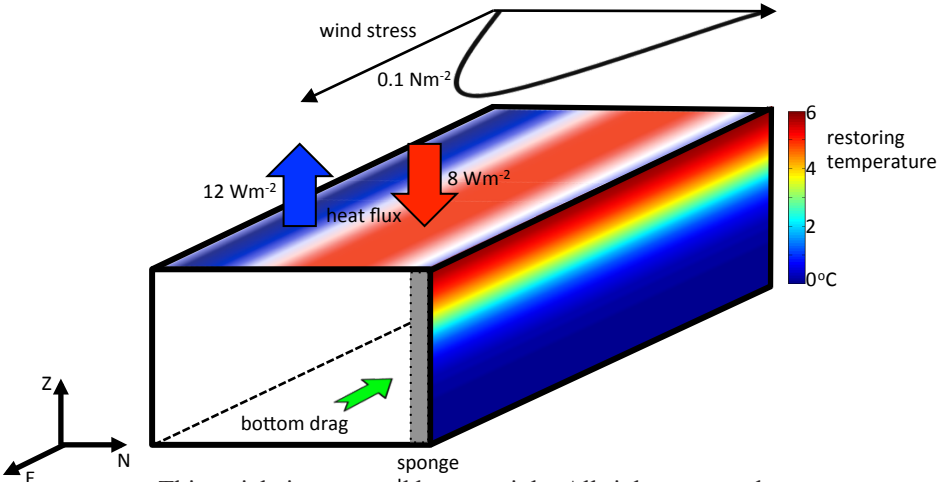

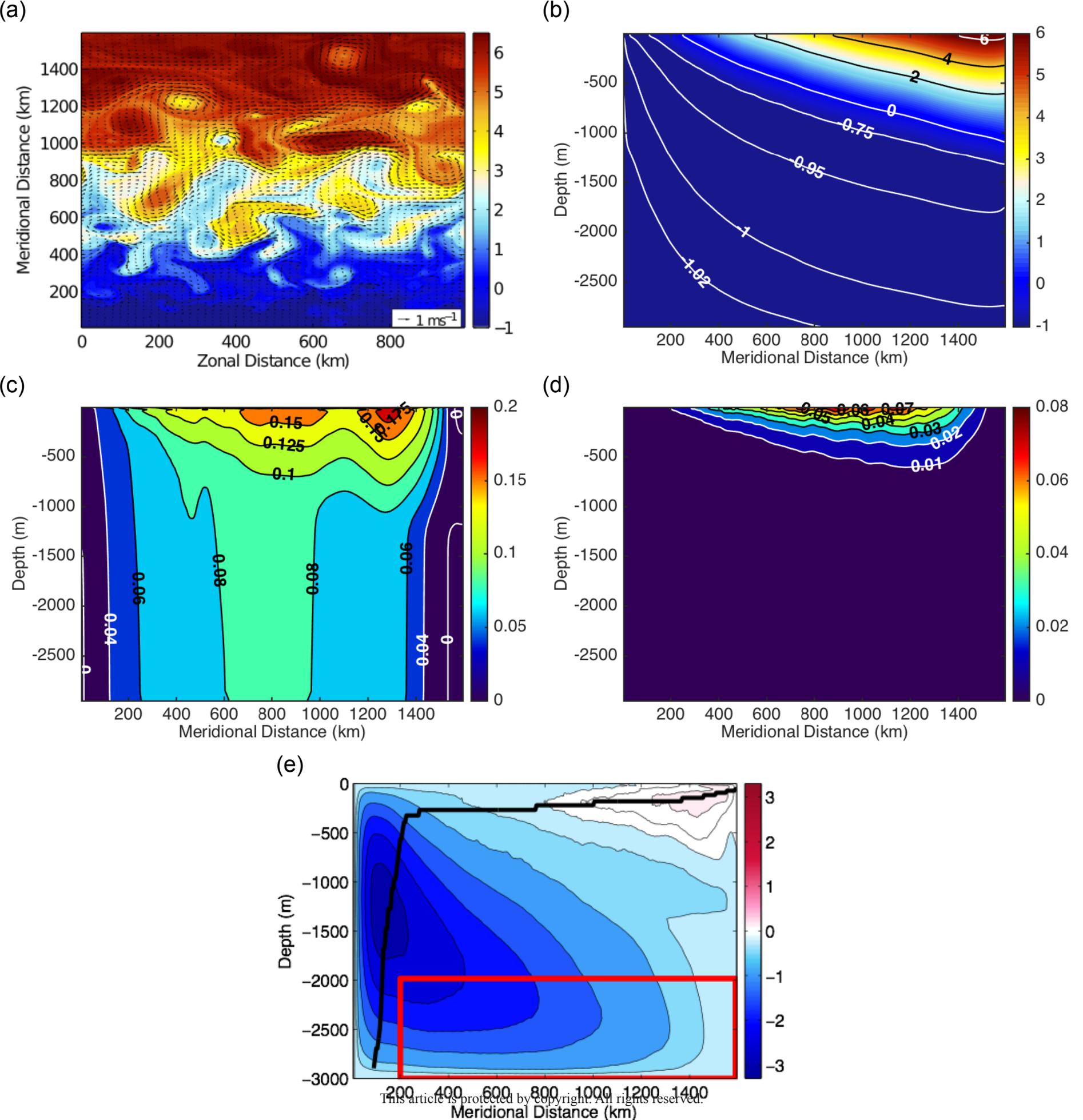

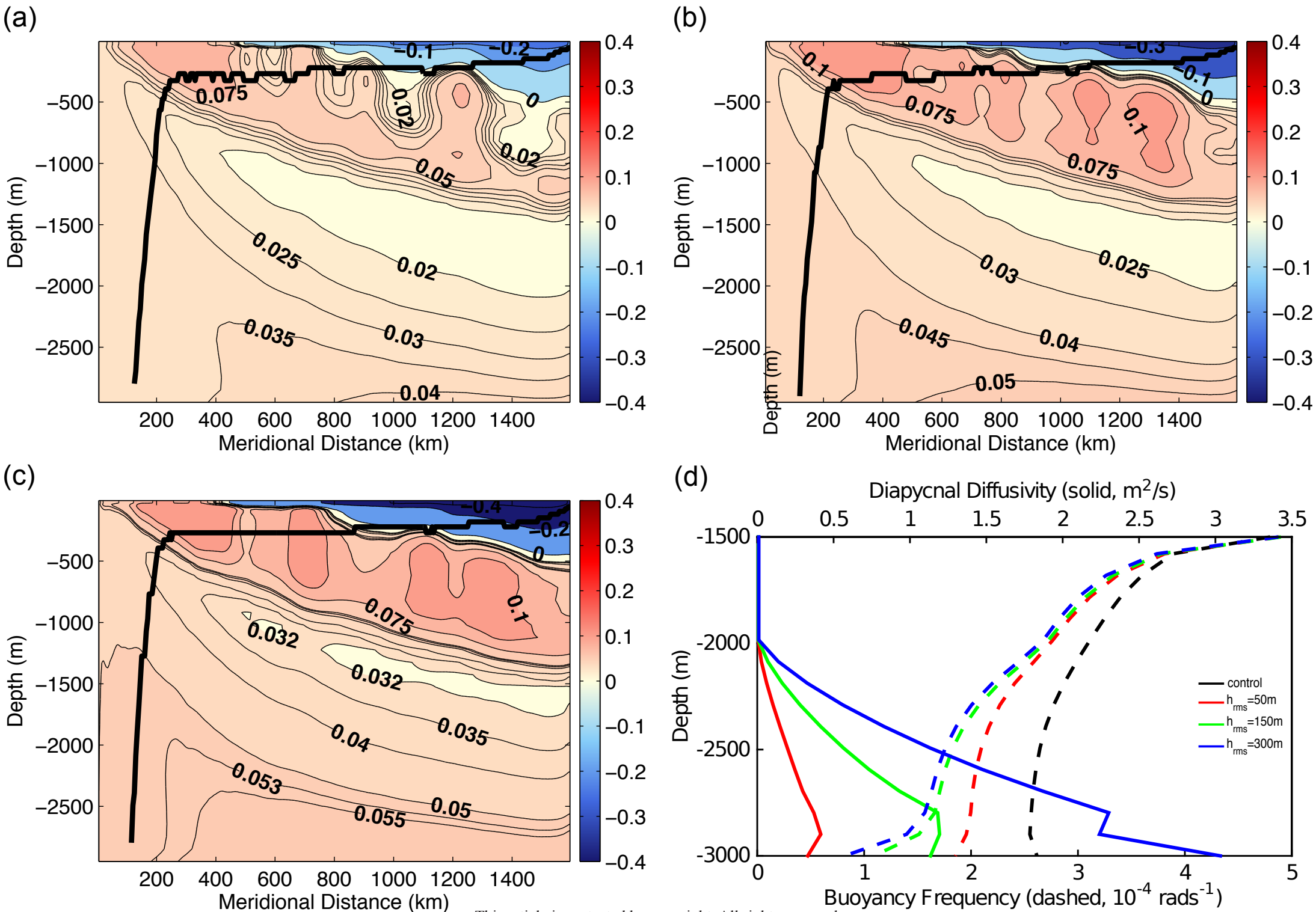

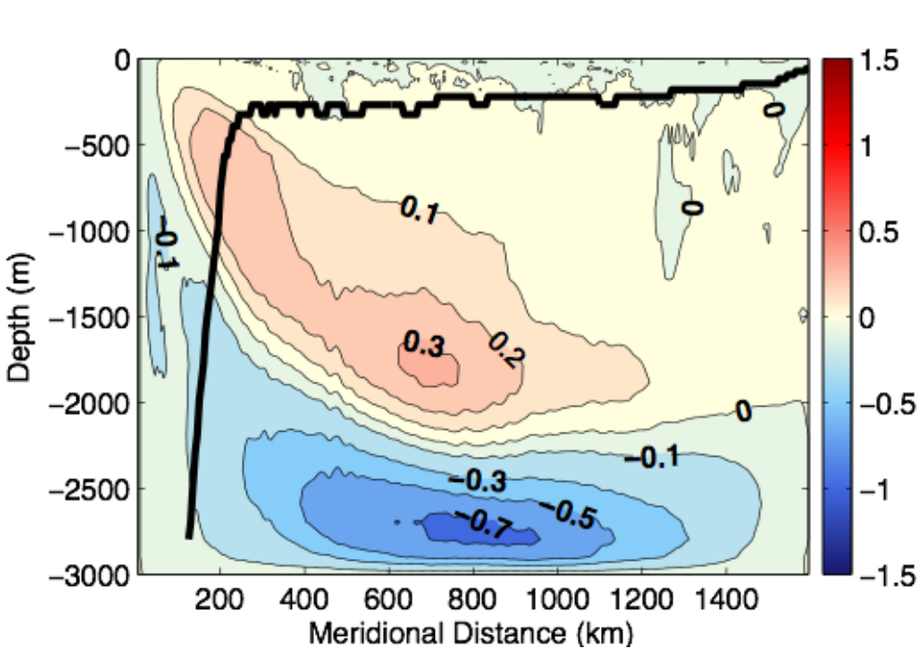

(d)

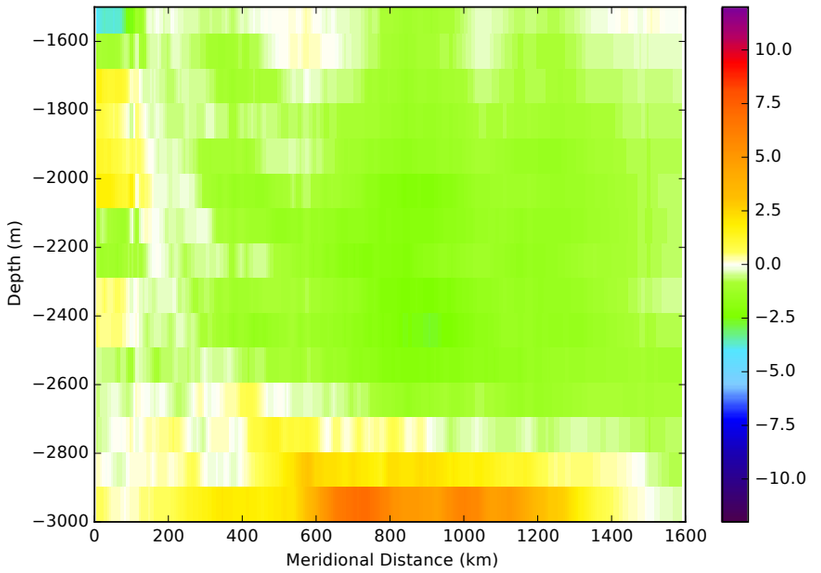

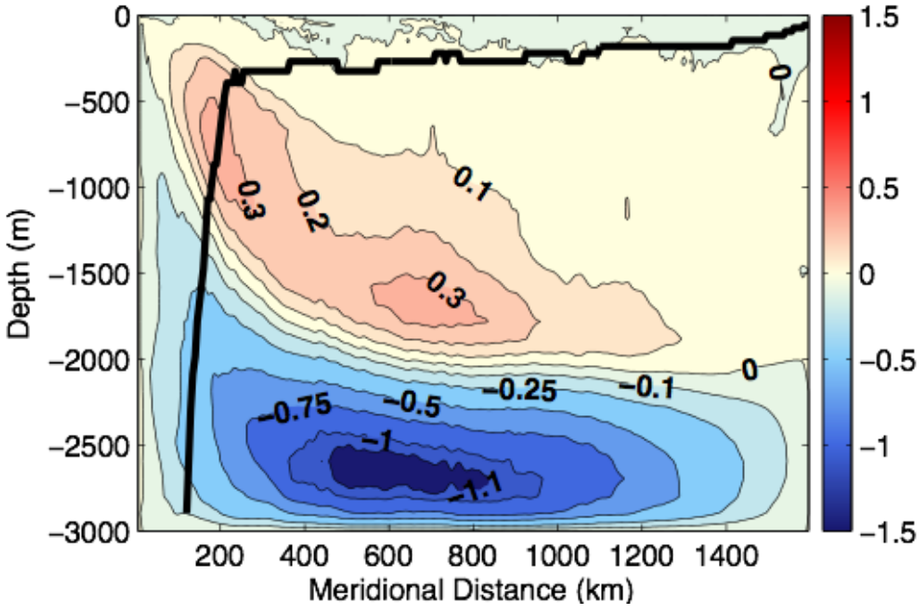

(e)

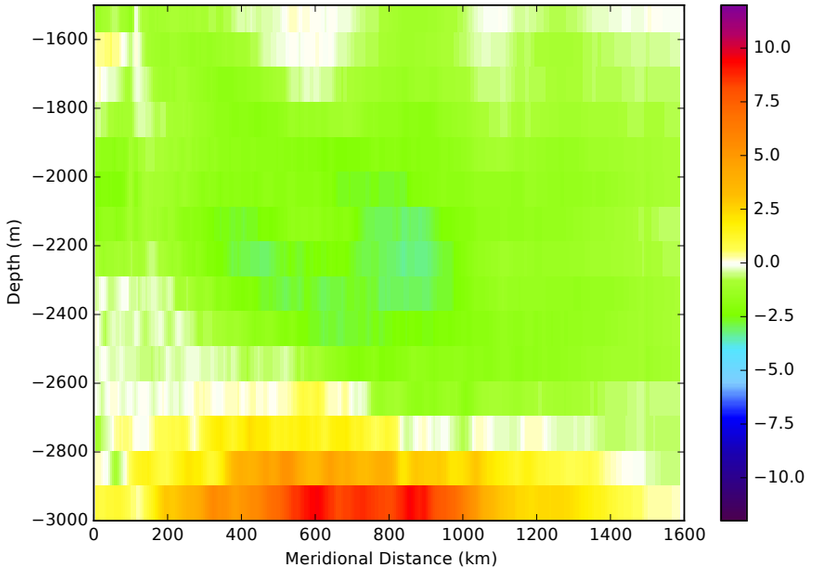

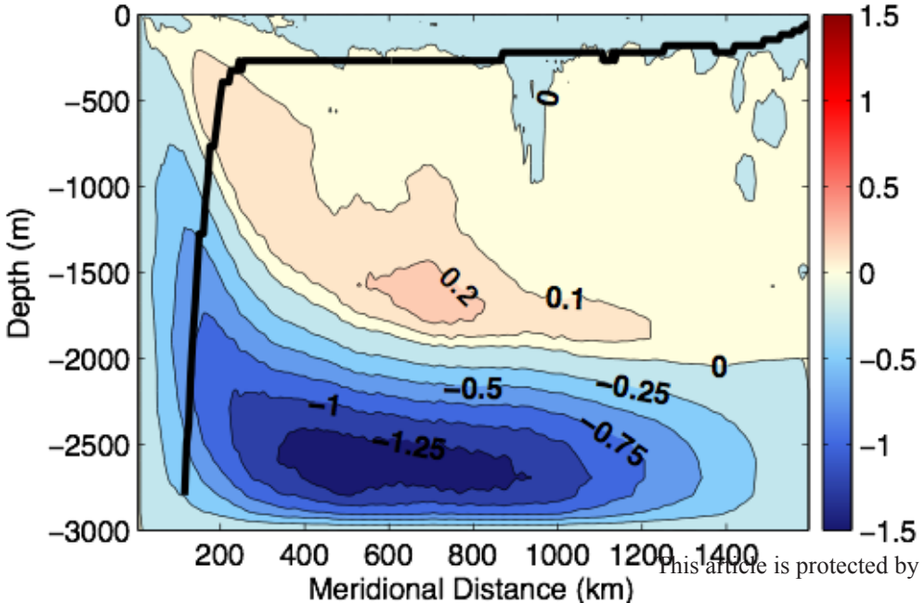

(f)